11-13-2008

Electromagnetic Modes in Cylindrical Structures

Jakub Pritz
University of South Florida

Electromagnetic Modes in Cylindrical Structures

by

Jakub Pritz

A thesis submitted in partial fulfillment
of the requirements for the degree of
Master of Science
Department of Physics
College of Arts and Sciences
University of South Florida

Major Professor: Lilia Woods, Ph.D.
Sarath Witanachchi, Ph.D.
Ivan Oleynik, Ph.D.

Date of Approval:
November 13, 2008

Keywords: Plasmon, Nanophotonics, Optical Properties, Dispersion, Concentric Layers

Table of Contents

List of Tables ii

List of Figures iii

Abstract iv

I. Introduction 1

II. Electromagnetic Modes 5

III. The Model 11

IV. The Non-Radiative Regime 19

V. The Radiative Regime 28

VI. Conclusions 37

References 40

Bibliography 44

List of Tables

Table 1	Characteristics of Different Plasmon Polariton Modes	7
Table 2	Constants used in the Silver Dielectric Function	19
Table 3	Constants used in the Carbon Nanotube Dielectric Function	34

List of Figures

Figure 1.	Illustration of Different Mode Types	8
Figure 2.	Multiwalled Concentric Cylindrical Layers	11
Figure 3.	Non-Radiative Dispersion Curves and Number of Layers	21
Figure 4.	Non-Radiative Dispersion Curves and Plasmon Frequency	23
Figure 5.	Non-Radiative Dispersion Curves and Thickness	24
Figure 6.	Non-Radiative Dispersion Curves and Changing Radii	25
Figure 7.	Non-Radiative Dispersion Curves and Changing one Radius	25
Figure 8.	Radiative Ag Dispersion Curves One Layers	29
Figure 9.	Radiative Ag Dispersion Curves Two Layers	31
Figure 10.	Radiative Ag Dispersion Curves Three Layers	33
Figure 11.	Radiation CN Dispersion Curves for Various Ns	35

Electromagnetic Modes in Cylindrical Structures

Jakub Pritz

ABSTRACT

Nanostructures have received much attention from the physical and engineering communities in the past few years. The understanding of the behavior of nanostructures in various conditions is warranted since the applications of such materials in optics, electronics, and mechanics is ever expanding. This thesis investigates a specific type of structure, a concentric cylindrical. More specifically, the dispersion relation of radiating and non-radiating plasmon polaritons (quasi-particles resulting from interactions of photons and surface electrons) is studied under varying conditions. We intend to show the influence of changing the thickness of the layers, the number of layers, the curvature of each layer, and the type of material the layers has on the dispersion relation.

By first solving Maxwell's equations in cylindrical coordinates and applying boundary conditions, we developed a matrix equation through which we were able to obtain the dispersion relation for an N layered cylindrical system characterized by a specified dielectric function placed into a background. For the non-radiative modes we used the bisection method to obtain the dispersion relation; however, since radiative modes encompass virtual modes, which contain real and imaginary components, a Newton method was used to gather that data. The dielectric functions for silver and carbon dielectric functions were used to describe the material layers within the radiative and non-radiative regimes.

The results show that curvature changes influence the surface plasmon polariton dispersion by either red shifting or blue shifting the energetics. Lifetimes and damping are seen to be influenced by the curvature as well. The addition of more layers to the system results in an increase in the complexity of the dispersion energetics.

The results obtained would help provide better scanning tips within the optical microscopy field. Also, these results can have direct application to the field of photonics. Finally, these results also help provide the foundations to understanding the fundamentals of long-ranged forces in cylindrical layered structures.

I. Introduction

Electromagnetic excitations have long been of interest to physicists. Beginning in the 1940's, Fano used a specific type of electromagnetic excitation, known as plasmon polaritons (PP), to explain the Wood's anomalies seen from metal diffraction gratings at optical frequencies (1). Ngai later extended this work (2) which confirmed previous experiments performed by Spicer (3) and Lander (4). Meanwhile, Fuchs and Kliewer added to the theoretical understanding by studying these excitations for ionic slab geometries (5, 6). Beck then used PPs to develop a dispersion relation for Al and Mg (7). Later, theoretical work took into account different geometries such as thin metallic films (8) and multilayers (9, 10). Today, PPs are still used for theoretical research when investigating plasmon hybridization in spherical nanoparticles (11) and when considering surface defects (12).

Experimentally, PPs were first seen in an electron energy loss experiment conducted by Powell, et al (13). Since then, PPs have been used in various experimental studies including: surface plasmon microscopy (14), bio-sensing (15), and electrochemistry (16). These excitations have also been observed optically (17, 18) and thus have found use in characterizing and measuring optical constants for metals (19).

The miniaturization of technology to the nanoscale regime is a fairly recent trend that has been gaining much interest. Materials can be made such that importance on their spatial dimensionality becomes a factor for material properties. For example, in two dimensions superlattices and thin films can be created using different techniques (20, 21). While constructing superlattices, nonlinear dielectric properties can be achieved making

application in voltage tunable devices available (22). One dimensional nanotubes have been shown to have high tensile strength (23). Nano-fibers, filaments, and wires (24) as well as quasi-one dimensional microtubules (25) and nanorods (26) have also been fabricated. Quasi-zero dimensional structures have been synthesized with examples being nanospheres (27) and nanodots (28). Zero dimensional structures are aptly suited in for use as fluorescence (29, 30) devices.

Research into the optical properties of these nanostructures has motivated the development of more efficient and novel devices. In particular, there has been much work done on one and quasi-one dimensional nanostructures and their optical properties. The study of infrared gaps for carbon nanotubes (31) could lead to more efficient thermal imaging devices. Knowledge of the optical response for nanocylinder arrays aids in the development of improved biological and chemical sensors (32). Electromagnetic excitations have also been investigated but mainly in simple cylindrical geometries such as: cylinders made from one material (33 – 36) and different dielectric layers (37 -39). However, not much theoretical investigation has gone into varying the geometry of cylindrical structures. With manufacturing techniques that can control the growth of single walled nanotubes (40), multiwalled nanotubes (41), vary the dielectric materials within cylindrical layers (42), and apply thin film coatings on nanotubes (43), the need to develop an understanding of the relationship between varying the cylindrical geometry and PP dispersion is validated.

Knowledge from these studies about electromagnetic modes has already led to development of useful devices. Optical switches (44), waveguides (45), and transmission of light through metallic layers (46) all rely on these modes. In fact, a term has been

given to the area of research for devices built based on plasmon properties: plasmonics. PP modes also serve as the basis for photonic circuits, the design of electronic circuits in the nanoscale regime (47).

As well as their applications, these electromagnetic excitations help to describe some fundamental forces of nature. The van der Waals and Casimir forces can both be determined from the electromagnetic modes of the materials present (48, 49). More specifically, the interaction energy between objects can be defined as the change in the zero point energy of the longitudinal electromagnetic modes of the system. These longitudinal modes are characterized by surface excitations (48). PPs also come into play when calculating reflectance, transmission, and absorption coefficients since these coefficients are effected by interaction of surface topology with electromagnetic waves. Therefore, a deep theoretical understanding of PP modes is warranted given the importance it has presented itself to the scientific field.

As stated before, fabrication of specific structures in the one and quasi-one dimensional regime is now possible; however, investigations of electromagnetic modes with varying cylindrical geometry have been limited. Electromagnetic modes also provide a fundamental role in the van der Waals and Casimir forces. Therefore, the goal of this paper is to provide a model for surface plasmon polariton (SPP) dispersion under a variety of cylindrical geometrical conditions such as varying number of layers (from single layered to three layers), varying the thickness of each layer, changing the inner and outer radii, and/or changing the dielectric material. There are two regimes for which these conditions were applied: the radiative and non-radiative regimes of the dispersion relation. The non-radiative regime are for those excitations whose momentum, $\hbar k$, is

greater than an excitation in vacuum that has the same frequency, ω; or simply, the non-radiative regime is to the right of the vacuum light line while the radiative regime is to the left (48). With this work, one will be able to better understand the roles PP modes play in energy distribution for cylindrical structures and how this varies with geometry; thus, construction of devices with this type of symmetry can benefit from these results.

II. Electromagnetic Modes

Electromagnetic fields immerse the world around us. They propagate via oscillations in the electric and magnetic fields as defined by Maxwell's equations:

$$\nabla \cdot \vec{E}(\vec{r},\omega) = \frac{\rho}{\varepsilon} \quad 1) \qquad \nabla \times \vec{E}(\vec{r},\omega) = -\frac{\partial \vec{B}(\vec{r},\omega)}{\partial t} \quad 3)$$

$$\nabla \cdot \vec{B}(\vec{r},\omega) = 0 \quad 2) \qquad \nabla \times \vec{B}(\vec{r},\omega) = \mu\varepsilon \frac{\partial \vec{E}(\vec{r},\omega)}{\partial t} \quad 4)$$

$\vec{E}$ and $\vec{B}$ are the electric and magnetic fields, respectively. Both can depend on the position, $\vec{r}$, and frequency, ω, of the excitation; μ is the permeability, ε is the permittivity, and ρ is the free electron density. Quanta of these electromagnetic oscillations are known as photons; these are the particles that carry the electromagnetic interactions between objects. Photons travel indefinitely until they interact with a new medium, defined by a change in either μ, ε, or ρ. Surfaces provide a natural place for these parameters to change, thus photons may interact with elements within this new medium. Light can transmit through without much change or even reflect off; however, due to electromagnetic interactions some of the photons interact along a thin layer of the surface. A portion of the energy of these photons is now contained along the surface; therefore, interfaces between objects of different dielectric property are capable of supporting energy from these photonic interactions.

Any sort of matter can support various types of excitations and particle modes. For example, the unit cell is the base structure for any crystalline system and its oscillation in time defines the two types of phonons, optical and acoustic. An acoustic phonon is a quantized vibration of the unit cell, while optical phonons have the elements

in the unit cell vibrating individually (50). Acoustic phonons always exist in medium, provided that the temperature does not equal zero. However, optical phonons require a finite amount of energy to be excited usually provided by electromagnetic radiation (48).

Another type of collective excitation, plasmons, strongly depend on the property of the medium. They are defined as quantized oscillations of the electron density within the material. An example of a quasi-particle supported by conductive materials is an exciton. They are defined by a one to one coupling between an electron and a hole through a Coulombic interaction.

A polariton results when a photon interacts with any charged excitation or particle in a quantized manner. These types of interactions occur when a photon changes a medium, i.e. passing through a surface or boundary. Continuity requires that the electric and magnetic fields on both sides of the interface be equal; this is expressed by the following boundary conditions:

$$(\overrightarrow{D_2} - \overrightarrow{D_1}) \cdot \hat{n} = \sigma \quad 5) \qquad \hat{n} \times (\overrightarrow{E_2} - \overrightarrow{E_1}) = 0 \quad 7)$$

$$(\overrightarrow{B_2} - \overrightarrow{B_1}) \cdot \hat{n} = 0 \quad 6) \qquad \hat{n} \times (\overrightarrow{H_2} - \overrightarrow{H_1}) = \vec{K} \quad 8)$$

Where $\overrightarrow{D}_{1,2} = \varepsilon_{1,2}\vec{E}_{1,2}$, $\overrightarrow{H}_{1,2} = \mu_{1,2}\vec{B}_{1,2}$, $\hat{n}$ is the unit vector perpendicular to the interface, σ is the surface charge density, and $\vec{K}$ is surface current. Interactions with different types of charged excitations in mediums are given specific names. For example, a polariton interacting with an optical phonon is called a phonon-polariton. Coupling an exciton with a polariton produces an exciton-polariton. Finally, when a quantized interaction occurs between a photon and a plasmon the name plasmon-polariton (PP) is given (48).

The focus of this work is to investigate PP interactions in a multilayered concentric cylindrical structure. There are two general regimes where this occurs in matter. For PPs, interactions within the bulk of an object result in bulk modes, while interactions occurring on the surface of an object result in what are called SPP.

Bulk modes, such as bulk plasmons and phonons, arise when there is a nonzero longitudinal electric field, the electric field parallel to the direction of motion, and the longitudinal current is taken to be zero. In a zero transverse electric field, where the field vector points perpendicular to the motion of the wave, coupled with a zero transverse current leads to a dispersion of light within the medium. The frequency of the interaction along with its associated wave number defines the dispersion of an interaction. Bulk modes arise from only taking into consideration Maxwell's equations within the medium; therefore, boundary conditions are not taken into consideration.

When boundary conditions are taken into consideration surface modes arise.

Mode	**Dielectric Function** $\varepsilon = \varepsilon' + i\,\varepsilon''$	
	Real Part	**Imaginary Part**
Fano	$\varepsilon' \leq -1$	$\varepsilon'' << \lvert \varepsilon' \rvert$
Evanescent	$-1 \leq \varepsilon' \leq 0$	$\varepsilon'' \approx \lvert \varepsilon' \rvert$
Brewster	$\varepsilon' \geq 0$	$\varepsilon'' << \lvert \varepsilon' \rvert$
Zenneck	$\varepsilon' << -1$	$\varepsilon'' >> \lvert \varepsilon' \rvert$

Table 1. Listing of the different mode characteristics. (48)

These boundary conditions, Eqs. 5-8, and the dielectric function define all the properties of surface modes. As shown in Table 1, the dielectric function helps to characterize these modes. The real part of the dielectric function is associated with energy stored in the medium; the imaginary portion of the dielectric function deals with dissipation. When there is no damping, $\varepsilon'' \rightarrow 0$, in the system, Fano modes are the only means of energy

propagation. Once damping is introduced, Brewster, Zenneck, and Evanescent modes replace Fano modes as means of energy propagation within the medium.

The four modes, Fano, Brewster, Evanescent, and Zenneck, are characterized by the dispersion relation, $\omega(\vec{k})$ (48). Brewster modes are bound to the surface of the medium. Evanescent modes decay rapidly. Zenneck modes are present in both the bulk and surface and so are rarely present in very thin materials. Fano modes are considered the true surface mode due to having a phase velocity less then the speed of light (48).

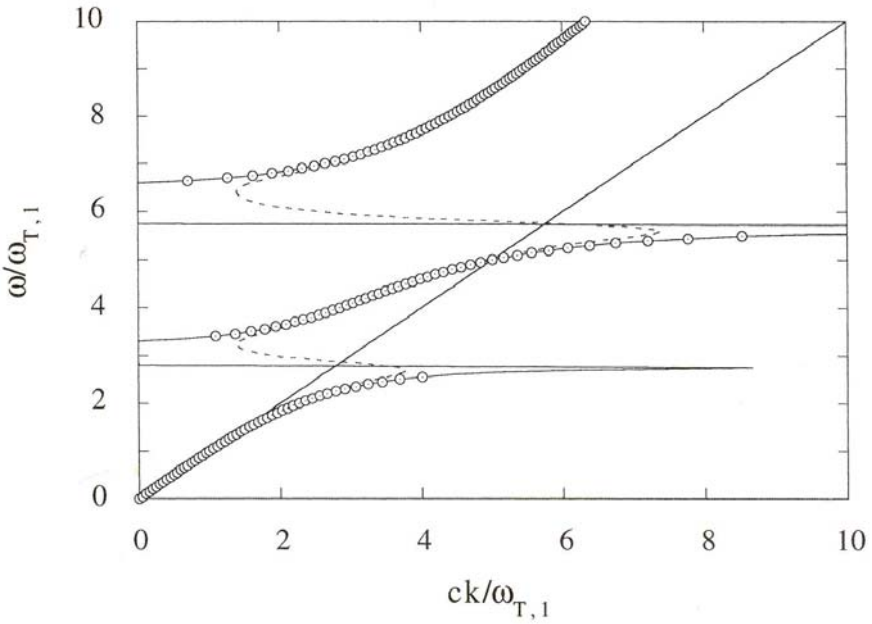

Figure 1. The solid and dashed curves are the dispersions of the modes without and with damping, respectively, when one demands that frequency is real valued. If one instead demands that $k/\omega_{T,1}$ is real valued the real part of the complex frequency follows the circles, even in the case of damping. (48)

Figure 1) shows the areas where the different surface modes occupy. The solid and dashed curves are the dispersions of these modes without and with damping, respectively. The circles are the real part of the complex frequency when k or ω is taken to be real valued. The circles follow the same pattern even in the presence of damping. The $\omega = ck$ line is the light line.

Because there are different characterizations for these modes, different applications can take advantage of the different PP modes. For example, ellipsometry (technique for finding dielectric properties of thin films) relies on Brewster and Fano modes (51) since these modes are strictly bound to the surface. Evanescent modes are useful for constructing bandpass filters (52); meanwhile, Brewster and Zenneck modes can assist light transmission in metallic films (53). Other optical microscopy techniques such as near-field microscopy can rely on all the types of modes (54, 55).

Since these modes are essentially energetic modes at the boundaries between objects, information about these modes will tell us much about the interactions between objects. For example, the stability of a structure can be gleaned from knowing how/what modes are propagating. Frictional forces between objects dictate ware and sheer stresses that occur at the interfaces of different materials. These frictional forces originate from electromagnetic interaction between the materials. Adhesion is another force resulting from electromagnetic bonding of two objects (56). Specifically, these forces result from van der Waal interactions and as will be shown, the van der Waal force results directly from the electromagnetic modes.

Vacuum fluctuations of the electromagnetic field in the vicinity of object boundaries give rise to surface area dependent forces. To study these forces, one needs to account for the interaction energy of boundaries and see how it changes as a function of object separation. This is exactly the same as taking the summed zero-point energy of electromagnetic modes and seeing how that changes as a function of object separation (56, 57). For example, in the van der Waal force one studies the interaction between

unpolarized atoms or molecules; while the Casimir force results from interactions of macroscopic objects (56).

To derive these modes, one must first start by expressing the electromagnetic radiation in mathematical terms. Maxwell's equations, Eqs. 1 – 4, provide this. Solving these partial differential equations for the $\vec{E}$ and $\vec{B}$ field will give the correct form one needs to have an expression for the electromagnetic radiation. The PP modes are then solved after the boundary conditions, Eqs. 5-8, have been applied to the electromagnetic expressions derived from Eqs. 1 – 4.

The procedure described above is a general way of obtaining the PP modes. This manuscript focuses on cylindrical geometries; therefore, it is more natural to express the solutions to Maxwell's equations and the applied boundary conditions within a cylindrical coordinate format. The next section will do this and describe the model used to obtain the dispersion relations for this cylindrical system. Geometry will play a key part in our model and influences of number of layers, curvature, and layer thickness will be described. Our model will take into consideration different dielectric functions as well.

III. The Model

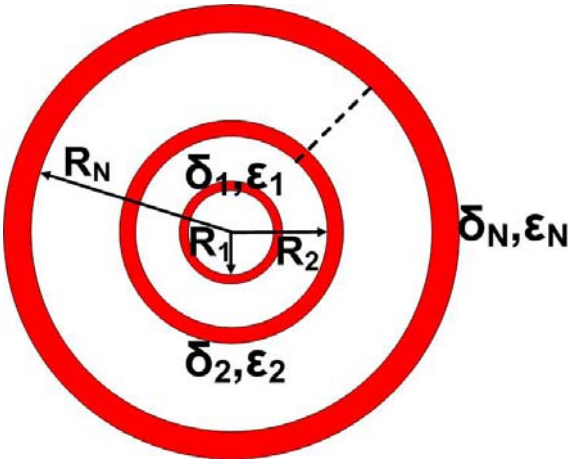

Figure 2. Multilayer concentric cylindrical layer system. There are N layers with radius R_j, thickness δ_i, and dielectric function $\varepsilon_i(\omega)$. The environment medium has a dielectric constant $\varepsilon_0(\omega)$. The z-axis is perpendicular to the page.

Since the goal of this manuscript is to develop a model for PP dispersion for a cylindrical geometry it is only natural to use cylindrical coordinates. Figure 2) displays the parameters we used to describe the structure under investigation. It is a cross section of a multiwalled cylinder displayed azimuthally. R_N represents the inner radius layer number N (counting from the inside to out). δ_N represents the thickness for each layer, while ε_N is the dielectric function for layer N.

$$\nabla^2 \vec{E}(\vec{r},\omega) - \frac{\omega^2}{c^2}\mu(\vec{r},\omega)\varepsilon(\vec{r},\omega)\vec{E}(\vec{r},\omega) = 0 \qquad 9)$$

$$\vec{E}(\vec{r},\omega) = \vec{E}(\vec{r})e^{-i\omega t} \qquad 10)$$

$$\vec{E}(\vec{r}) = \vec{E}(\rho,\theta)e^{-i\omega t}e^{ikz} \qquad 11)$$

$$\nabla^2 \vec{E}(\vec{r},\omega) = \nabla_\perp^2 \vec{E}(\vec{r},\omega) + \frac{\partial^2 \vec{E}(\vec{r},\omega)}{\partial z^2} \qquad 12)$$

As stated before, the solutions to Maxwell's equations will be solved for in cylindrical coordinates *(r, z, θ)*. The wave equation, Eq. 9, is derived from Maxwell's equations, Eqs. 1 - 4. Next, we assume an electric field form that can be separated into spatial and time dependent values, Eq. 10, and has the form shown in Eq. 11. The Laplacian part of Eq. 9 is split into its perpendicular and *z* parts as defined in Eq. 12.

$$(\nabla_{\perp}^2 + \chi_j^2)\vec{E}(\rho,\theta)e^{ikz}e^{-i\omega t} = 0 \qquad 13)$$

Here $\chi_j^2 = \frac{\varepsilon_j \mu_j}{c^2}\omega^2 - k^2$. Using Eqs. 9 - 13, we find the solutions for the $\vec{E}(\rho,\theta)$ and $\vec{B}(\rho,\theta)$ fields in each region *j*. Each field has three components: *ρ*, *θ*, and *z*. Results for $\vec{E}(\rho,\theta)$ and $\vec{B}(\rho,\theta)$ are:

$$E_z^j = \sum_{n=0}^{\infty}\{C_n^j f_n(\chi_j\rho_j) + F_n^j g_n(\chi_j\rho_j)\}e^{in\theta}e^{i(kz-\omega t)} \qquad 14)$$

$$E_\theta^j = \sum_{n=0}^{\infty}\{\frac{-kn}{\chi_j^2\rho_j}(C_n^j f_n(\chi_j\rho_j) + F_n^j g_n(\chi_j\rho_j)) - \frac{i\omega}{\chi_j}(D_n^j f_n'(\chi_j\rho_j) + G_n^j g_n'(\chi_j\rho_j)) \qquad 15)$$

$$E_\rho^j = \sum_{n=0}^{\infty}\{\frac{-n\omega}{\chi_j^2\rho_j}(D_n^j f_n(\chi_j\rho_j) + G_n^j g_n(\chi_j\rho_j)) + \frac{ik}{\chi_j}(C_n^j f_n'(\chi_j\rho_j) + F_n^j g_n'(\chi_j\rho_j)\} \qquad 16)$$

$$B_z^j = \sum_{n=0}^{\infty}\{D_n^j f_n(\chi_j\rho_j) + G_n^j g_n(\chi_j\rho_j)\}e^{in\theta}e^{i(kz-\omega t)} \qquad 17)$$

$$B_\theta^j = \sum_{n=0}^{\infty}\{\frac{-kn}{\chi_j^2\rho_j}(D_n^j f_n(\chi_j\rho_j) + G_n^j g_n(\chi_j\rho_j)) + \frac{i\varepsilon_j\mu_j\omega}{\chi_j}(C_n^j f_n'(\chi_j\rho_j) + F_n^j g_n'(\chi_j\rho_j))\} \qquad 18)$$

$$B_\rho^j = \sum_{n=0}^{\infty}\{\frac{n\varepsilon_j\mu_j\omega}{\chi_j^2\rho_j}(C_n^j f_n(\chi_j\rho_j) + F_n^j g_n(\chi_j\rho_j)) + \frac{ik}{\chi_j}(D_n^j f_n'(\chi_j\rho_j) + G_n^j g_n'(\chi_j\rho_j)\} \qquad 19)$$

Eqs. 14 - 19 show these results for each coordinate *z*, *θ*, and *ρ*, for the electric and magnetic field (note the symbols for vector representation have been dropped). ρ_j is the

radial vector for layer j (Figure 2)), ε_j is the dielectric function, k is the wave number, and ω is the frequency. In this work we consider only non-magnetic materials thus $\mu_j = 1$ everywhere. C_n^j, D_n^j, F_n^j, and G_n^j are unknown coefficients which will be solved for later. The terms f and g are substitutes for Bessel and Hankel functions with argument $\chi_j\rho_j$. Depending on the regime being considered, f and g represent different functions. More specifically, when in the radiative regime, $f_n(\chi_j\rho_j) = J_n(\chi_j\rho_j)$ and $g_n(\chi_j\rho_j) = H_n^1(\chi_j\rho_j)$; for the non-radiative regime, $f_n(\chi_j\rho_j) = I_n(\chi_j\rho_j)$ and $g_n(\chi_j\rho_j) = K_n(\chi_j\rho_j)$. Consequently, $g_n^{'} = \frac{\partial g}{\partial(\chi_j\rho_j)}$ and likewise $f_n^{'} = \frac{\partial f}{\partial(\chi_j\rho_j)}$. Finally, n represents the order of the Bessel and/or Hankel function used.

As described earlier, the next step is to apply boundary conditions to solve for the coefficients: C_n^j, D_n^j, F_n^j, and G_n^j. The boundary conditions for cylindrical coordinates are:

$$E_\theta^j(\rho_j) = E_\theta^{j+1}(\rho_j) \quad 20) \qquad B_\theta^j(\rho_j) = B_\theta^{j+1}(\rho_j) \quad 23)$$

$$\varepsilon_j E_\rho^j(\rho_j) = \varepsilon_{j+1} E_\rho^{j+1}(\rho_j) \quad 21) \qquad B_\rho^j(\rho_j) = B_\rho^{j+1}(\rho_j) \quad 24)$$

$$E_z^j(\rho_j) = E_z^{j+1}(\rho_j) \quad 22) \qquad \frac{1}{\mu_j} B_z^j(\rho_j) = \frac{1}{\mu_{j+1}} B_z^{j+1}(\rho_j) \quad 25)$$

Note, since there are only four coefficients, one needs to only use four of the boundary conditions to write equations for the coefficients. The result of applying the boundary conditions and solving for the coefficients leads to:

$$C_n^{j+1} = \frac{1}{\Delta_{j+1}}\{(\frac{\chi_{j+1}\varepsilon_j}{\varepsilon_{j+1}\chi_j} f_n^{'}(\chi_j R_j) g_n(\chi_{j+1} R_j) - f_n(\chi_j R_j) g_n^{'}(\chi_{j+1} R_j))\mathbf{C_n^j}$$

$$+(\frac{\chi_{j+1}\varepsilon_j}{\varepsilon_{j+1}\chi_j} g_n^{'}(\chi_j R_j) g_n(\chi_{j+1} R_j) - g_n(\chi_j R_j) g_n^{'}(\chi_{j+1} R_j))\mathbf{F_n^j} \qquad 26)$$

$$+\frac{i\chi_{j+1} n\omega}{k\varepsilon_{j+1} R_j}(\frac{\varepsilon_j}{\chi_j^2} - \frac{\varepsilon_{j+1}}{\chi_{j+1}^2})(f_n(\chi_j R_j) g_n(\chi_{j+1} R_j)\mathbf{D_n^j} + g_n(\chi_j R_j) g_n(\chi_{j+1} R_j)\mathbf{G_n^j})\}$$

$$F_n^{j+1} = \frac{-1}{\Delta_{j+1}}\{(\frac{\chi_{j+1}\varepsilon_j}{\varepsilon_{j+1}\chi_j} f_n^{'}(\chi_j R_j) f_n(\chi_{j+1} R_j) - f_n(\chi_j R_j) f_n^{'}(\chi_{j+1} R_j))\mathrm{C_n^j}$$

$$+(\frac{\chi_{j+1}\varepsilon_j}{\varepsilon_{j+1}\chi_j} g_n^{'}(\chi_j R_j) f_n(\chi_{j+1} R_j) - g_n(\chi_j R_j) f_n^{'}(\chi_{j+1} R_j))\mathrm{F_n^j} \qquad 27)$$

$$+\frac{i\chi_{j+1} n\omega}{k\varepsilon_{j+1} R_j}(\frac{\varepsilon_j}{\chi_j^2} - \frac{\varepsilon_{j+1}}{\chi_{j+1}^2})(f_n(\chi_j R_j) f_n(\chi_{j+1} R_j)\mathrm{D_n^j} + g_n(\chi_j R_j) f_n(\chi_{j+1} R_j)\mathrm{G_n^j})\}$$

$$D_n^{j+1} = \frac{1}{\Delta_{j+1}}\{-\frac{ink\chi_{j+1}}{R_j\omega}(\frac{1}{\chi_j^2} - \frac{1}{\chi_{j+1}^2})(f_n(\chi_j R_j) g_n(\chi_{j+1} R_j)\mathrm{C_n^j} + g_n(\chi_j R_j) g_n(\chi_{j+1} R_j)\mathrm{F_n^j})$$

$$+(\frac{\chi_{j+1}}{\chi_j} f_n^{'}(\chi_j R_j) g_n(\chi_{j+1} R_j) - f_n(\chi_j R_j) g_n^{'}(\chi_{j+1} R_j))\mathrm{D_n^j} \qquad 28)$$

$$+(\frac{\chi_{j+1}}{\chi_j} g_n^{'}(\chi_j R_j) g_n(\chi_{j+1} R_j) - g_n(\chi_j R_j) g_n^{'}(\chi_{j+1} R_j))\mathrm{G_n^j}\}$$

$$G_n^{j+1} = \frac{-1}{\Delta_{j+1}}\{-\frac{ink\chi_{j+1}}{R_j\omega}(\frac{1}{\chi_j^2} - \frac{1}{\chi_{j+1}^2})(f_n(\chi_j R_j) f_n(\chi_{j+1} R_j)\mathrm{C_n^j} + g_n(\chi_j R_j) f_n(\chi_{j+1} R_j)\mathrm{F_n^j})$$

$$+(\frac{\chi_{j+1}}{\chi_j} f_n^{'}(\chi_j R_j) f_n(\chi_{j+1} R_j) - f_n(\chi_j R_j) f_n^{'}(\chi_{j+1} R_j))\mathrm{D_n^j} \qquad 29)$$

$$+(\frac{\chi_{j+1}}{\chi_j} g_n^{'}(\chi_j R_j) f_n(\chi_{j+1} R_j) - g_n(\chi_j R_j) f_n^{'}(\chi_{j+1} R_j))\mathrm{G_n^j}\}$$

Where $\Delta_{j+1} = f_n'(\chi_{j+1}R_j)g_n(\chi_{j+1}R_j) - f_n(\chi_{j+1}R_j)g_n'(\chi_{j+1}R_j)$. These equations were solved for the outer layer coefficients in terms of the inner layer coefficients. Similar results would be obtained in solving for the inside layer coefficients in terms of the outer layer coefficients; however, every "*j + 1*" → "*j*" and every "*j*" → "*j + 1*."

The coefficients can be arranged into the following matrix form:

$$\begin{pmatrix} C_n^{j+1} \\ D_n^{j+1} \\ F_n^{j+1} \\ G_n^{j+1} \end{pmatrix} = \begin{pmatrix} \alpha_{n,C}^{j+1,j} & \beta_{n,C}^{j+1,j} & \gamma_{\mathbf{n,C}}^{\mathbf{j+1,j}} & \lambda_{\mathbf{n,C}}^{\mathbf{j+1,j}} \\ \alpha_{n,D}^{j+1,j} & \beta_{n,D}^{j+1,j} & \gamma_{\mathbf{n,D}}^{\mathbf{j+1,j}} & \lambda_{\mathbf{n,D}}^{\mathbf{j+1,j}} \\ \alpha_{n,F}^{j+1,j} & \beta_{n,F}^{j+1,j} & \gamma_{\mathbf{n,F}}^{\mathbf{j+1,j}} & \lambda_{\mathbf{n,F}}^{\mathbf{j+1,j}} \\ \alpha_{n,G}^{j+1,j} & \beta_{n,G}^{j+1,j} & \gamma_{\mathbf{n,G}}^{\mathbf{j+1,j}} & \lambda_{\mathbf{n,G}}^{\mathbf{j+1,j}} \end{pmatrix} \begin{pmatrix} C_n^j \\ D_n^j \\ F_n^j \\ G_n^j \end{pmatrix} \quad 30)$$

Where the following substitutions have been made:

$$\alpha_{n,C}^{j+1} = \frac{1}{\Delta_{j+1}}[\frac{\chi_{j+1}\varepsilon_j}{\varepsilon_{j+1}\chi_j} f_n'(\chi_j\rho_j)g_n(\chi_{j+1}\rho_j) - f_n(\chi_j\rho_j)g_n'(\chi_{j+1}\rho_j)] \quad 31)$$

$$\beta_{n,C}^{j+1} = \frac{1}{\Delta_{j+1}} \frac{in\chi_{j+1}}{\kappa\varepsilon_{j+1}\rho_j} \left[\frac{\varepsilon_j}{\chi_j^{\,2}} - \frac{\varepsilon_{j+1}}{\chi_{j+1}^{\,2}} \right] f_n(\chi_j\rho_j)g_n(\chi_{j+1}\rho_j) \quad 32)$$

$$\gamma_{n,C}^{j+1} = \frac{1}{\Delta_{j+1}} \left[\frac{\chi_{j+1}\varepsilon_j}{\varepsilon_{j+1}\chi_j} g_n'(\chi_j\rho_j)g_n(\chi_{j+1}\rho_j) - g_n(\chi_j\rho_j)g_n'(\chi_{j+1}\rho_j) \right] \quad 33)$$

$$\lambda_{n,C}^{j+1} = \frac{1}{\Delta_{j+1}} \frac{in\chi_{j+1}}{\kappa\varepsilon_{j+1}\rho_j} \left[\frac{\varepsilon_j}{\chi_j^{\,2}} - \frac{\varepsilon_{j+1}}{\chi_{j+1}^{\,2}} \right] g_n(\chi_j\rho_j)g_n(\chi_{j+1}\rho_j) \quad 34)$$

$$\alpha_{n,D}^{j+1} = \frac{-1}{\Delta_{j+1}} \frac{in\chi_{j+1}\kappa}{\rho_j\omega} \left[\frac{1}{\chi_j^{\,2}} - \frac{1}{\chi_{j+1}^{\,2}} \right] f_n(\chi_j\rho_j)g_n(\chi_{j+1}\rho_j) \quad 35)$$

$$\beta_{n,D}^{j+1} = \frac{1}{\Delta_{j+1}} \left[\frac{\chi_{j+1}}{\chi_j} f_n'(\chi_j\rho_j)g_n(\chi_{j+1}\rho_j) - f_n(\chi_j\rho_j)g_n'(\chi_{j+1}\rho_j) \right] \quad 36)$$

$$\gamma_{n,D}^{j+1} = \frac{-1}{\Delta_{j+1}} \frac{in\chi_{j+1}\kappa}{\rho_j\omega} \left[\frac{1}{\chi_j^{\,2}} - \frac{1}{\chi_{j+1}^{\,2}} \right] g_n(\chi_j\rho_j)g_n(\chi_{j+1}\rho_j) \quad 37)$$

$$\lambda_{n,D}^{j+1} = \frac{1}{\Delta_{j+1}}\left[\frac{\chi_{j+1}}{\chi_j} g_n'(\chi_j\rho_j) g_n(\chi_{j+1}\rho_j) - g_n(\chi_j\rho_j) g_n'(\chi_{j+1}\rho_j)\right] \quad 38)$$

$$\alpha_{n,F}^{j+1} = \frac{-1}{\Delta_{j+1}}\left[\frac{\chi_{j+1}\varepsilon_j}{\varepsilon_{j+1}\chi_j} f_n'(\chi_j\rho_j) f_n(\chi_{j+1}\rho_j) - f_n(\chi_j\rho_j) f_n'(\chi_{j+1}\rho_j)\right] \quad 39)$$

$$\beta_{n,F}^{j+1} = \frac{-1}{\Delta_{j+1}} \frac{in\chi_{j+1}}{\kappa\varepsilon_{j+1}\rho_j}\left[\frac{\varepsilon_j}{\chi_j^{\,2}} - \frac{\varepsilon_{j+1}}{\chi_{j+1}^{\,2}}\right] f_n(\chi_j\rho_j) f_n(\chi_{j+1}\rho_j) \quad 40)$$

$$\gamma_{n,F}^{j+1} = \frac{-1}{\Delta_{j+1}}\left[\frac{\chi_{j+1}\varepsilon_j}{\varepsilon_{j+1}\chi_j} g_n'(\chi_j\rho_j) f_n(\chi_{j+1}\rho_j) - g_n(\chi_j\rho_j) f_n'(\chi_{j+1}\rho_j)\right] \quad 41)$$

$$\lambda_{n,F}^{j+1} = \frac{-1}{\Delta_{j+1}} \frac{in\chi_{j+1}}{\kappa\varepsilon_{j+1}\rho_j}\left[\frac{\varepsilon_j}{\chi_j^{\,2}} - \frac{\varepsilon_{j+1}}{\chi_{j+1}^{\,2}}\right] g_n(\chi_j\rho_j) f_n(\chi_{j+1}\rho_j) \quad 42)$$

$$\alpha_{n,G}^{j+1} = \frac{1}{\Delta_{j+1}} \frac{in\chi_{j+1}\kappa}{\rho_j\omega}\left[\frac{1}{\chi_j^{\,2}} - \frac{1}{\chi_{j+1}^{\,2}}\right] f_n(\chi_j\rho_j) f_n(\chi_{j+1}\rho_j) \quad 43)$$

$$\beta_{n,G}^{j+1} = \frac{-1}{\Delta_{j+1}}\left[\frac{\chi_{j+1}}{\chi_j} f_n'(\chi_j\rho_j) f_n(\chi_{j+1}\rho_j) - f_n(\chi_j\rho_j) f_n'(\chi_{j+1}\rho_j)\right] \quad 44)$$

$$\gamma_{n,G}^{j+1} = \frac{1}{\Delta_{j+1}} \frac{in\chi_{j+1}\kappa}{\rho_j\omega}\left[\frac{1}{\chi_j^{\,2}} - \frac{1}{\chi_{j+1}^{\,2}}\right] g_n(\chi_j\rho_j) f_n(\chi_{j+1}\rho_j) \quad 45)$$

$$\lambda_{n,G}^{j+1} = \frac{-1}{\Delta_{j+1}}\left[\frac{\chi_{j+1}}{\chi_j} g_{nn}'(\chi_j\rho_j) f_n(\chi_{j+1}\rho_j) - g_n'(\chi_j\rho_j) f_n'(\chi_{j+1}\rho_j)\right] \quad 46)$$

One can now write a matrix equation that couples the first layer with the second, the second with the third, third with the fourth, etc. Therefore, one can couple the inner layer with the outermost layer and because of the simple switching of indices one has a relation between the outermost layer and the innermost. For purposes of solving for the dispersion relation, it will be convenient to write the innermost layer with itself going up through the layers and back down. The following shows this process to layer *N* and back.

$$\begin{pmatrix} C_n^1 \\ D_n^1 \\ F_n^1 \\ G_n^1 \end{pmatrix} = \begin{pmatrix} \alpha_{n,C}^{1,2} & \beta_{n,C}^{1,2} & \gamma_{\mathrm{n,C}}^{1,2} & \lambda_{n,C}^{1,2} \\ \alpha_{n,D}^{1,2} & \beta_{n,D}^{1,2} & \gamma_{\mathrm{n,D}}^{1,2} & \lambda_{n,D}^{1,2} \\ \alpha_{n,F}^{1,2} & \beta_{n,F}^{1,2} & \gamma_{\mathrm{n,F}}^{1,2} & \lambda_{n,F}^{1,2} \\ \alpha_{n,G}^{1,2} & \beta_{n,G}^{1,2} & \gamma_{\mathrm{n,G}}^{1,2} & \lambda_{n,G}^{1,2} \end{pmatrix} \times \begin{pmatrix} \alpha_{n,C}^{2,3} & \beta_{n,C}^{2,3} & \gamma_{\mathrm{n,C}}^{2,3} & \lambda_{\mathrm{n,C}}^{2,3} \\ \alpha_{n,D}^{2,3} & \beta_{n,D}^{2,3} & \gamma_{\mathrm{n,D}}^{2,3} & \lambda_{\mathrm{n,D}}^{2,3} \\ \alpha_{n,F}^{2,3} & \beta_{n,F}^{2,3} & \gamma_{\mathrm{n,F}}^{2,3} & \lambda_{\mathrm{n,F}}^{2,3} \\ \alpha_{n,G}^{2,3} & \beta_{n,G}^{2,3} & \gamma_{\mathrm{n,G}}^{2,3} & \lambda_{\mathrm{n,G}}^{2,3} \end{pmatrix} \times \ldots$$

$$\times \begin{pmatrix} \alpha_{n,C}^{2N,2N+1} & \beta_{\mathrm{n,C}}^{2N,2N+1} & \gamma_{n,C}^{2N,2N+1} & \lambda_{\mathrm{n,C}}^{2N,2N+1} \\ \alpha_{n,D}^{2N,2N+1} & \beta_{\mathrm{n,D}}^{2N,2N+1} & \gamma_{n,D}^{2N,2N+1} & \lambda_{\mathrm{n,D}}^{2N,2N+1} \\ \alpha_{n,F}^{2N,2N+1} & \beta_{\mathrm{n,F}}^{2N,2N+1} & \gamma_{n,F}^{2N,2N+1} & \lambda_{\mathrm{n,F}}^{2N,2N+1} \\ \alpha_{n,G}^{2N,2N+1} & \beta_{\mathrm{n,G}}^{2N,2N+1} & \gamma_{n,G}^{2N,2N+1} & \lambda_{\mathrm{n,G}}^{2N,2N+1} \end{pmatrix} \times \begin{pmatrix} \alpha_{n,C}^{2N+1,2N} & \beta_{n,C}^{2N+1,2N} & \gamma_{\mathrm{n,C}}^{2N+1,2N} & \lambda_{\mathrm{n,C}}^{2N+1,2N} \\ \alpha_{n,D}^{2N+1,2N} & \beta_{n,D}^{2N+1,2N} & \gamma_{\mathrm{n,D}}^{2N+1,2N} & \lambda_{\mathrm{n,D}}^{2N+1,2N} \\ \alpha_{n,F}^{2N+1,2N} & \beta_{n,F}^{2N+1,2N} & \gamma_{\mathrm{n,F}}^{2N+1,2N} & \lambda_{\mathrm{n,F}}^{2N+1,2N} \\ \alpha_{n,G}^{2N+1,2N} & \beta_{n,G}^{2N+1,2N} & \gamma_{\mathrm{n,G}}^{2N+1,2N} & \lambda_{\mathrm{n,G}}^{2N+1,2N} \end{pmatrix} \times \ldots$$

$$\times \begin{pmatrix} \alpha_{n,C}^{3,2} & \beta_{n,C}^{3,2} & \gamma_{\mathrm{n,C}}^{3,2} & \lambda_{\mathrm{n,C}}^{\mathrm{j+1,j}} \\ \alpha_{n,D}^{3,2} & \beta_{n,D}^{3,2} & \gamma_{\mathrm{n,D}}^{3,2} & \lambda_{\mathrm{n,D}}^{\mathrm{j+1,j}} \\ \alpha_{n,F}^{3,2} & \beta_{n,F}^{3,2} & \gamma_{\mathrm{n,F}}^{3,2} & \lambda_{\mathrm{n,F}}^{\mathrm{j+1,j}} \\ \alpha_{n,G}^{3,2} & \beta_{n,G}^{3,2} & \gamma_{\mathrm{n,G}}^{3,2} & \lambda_{\mathrm{n,G}}^{\mathrm{j+1,j}} \end{pmatrix} \times \begin{pmatrix} \alpha_{n,C}^{2,1} & \beta_{\mathrm{n,C}}^{2,1} & \gamma_{n,C}^{2,1} & \lambda_{\mathrm{n,C}}^{2,1} \\ \alpha_{n,D}^{2,1} & \beta_{\mathrm{n,D}}^{2,1} & \gamma_{n,D}^{2,1} & \lambda_{\mathrm{n,D}}^{2,1} \\ \alpha_{n,F}^{2,1} & \beta_{\mathrm{n,F}}^{2,1} & \gamma_{n,F}^{2,1} & \lambda_{\mathrm{n,F}}^{2,1} \\ \alpha_{n,G}^{2,1} & \beta_{\mathrm{n,G}}^{2,1} & \gamma_{n,G}^{2,1} & \lambda_{\mathrm{n,G}}^{2,1} \end{pmatrix} \begin{pmatrix} C_n^1 \\ D_n^1 \\ F_n^1 \\ G_n^1 \end{pmatrix} \qquad 47)$$

For the non-radiative regime: $\alpha_{n,F,G}^{1,2}$, $\beta_{n,F,G}^{1,2}$, $\gamma_{\mathrm{n,F,G}}^{1,2}$, $\lambda_{n,F,G}^{1,2}$, $\alpha_{n,C,D,F,G}^{2N,2N+1}$, $\beta_{n,C,D,F,G}^{2N,2N+1}$, $\alpha_{n,C,D}^{2N+1,2N}$, $\beta_{n,C,D}^{2N+1,2N}$, $\gamma_{\mathrm{n,C,D}}^{2N+1,2N}$, $\lambda_{\mathrm{n,C,D}}^{2N+1,2N}$, $\gamma_{n,C,D,F,G}^{2,1}$, and $\lambda_{\mathrm{n,C,\,D,\,F,\,G}}^{2,1}$ are all zero within Eq. 47. The zeroes are required from the continuity of the modified Bessel functions at $\rho \rightarrow 0$ and $\rho \rightarrow \infty$. The limiting conditions are different for the radiative regime since the Bessel and Hankel functions used are substituted in for the f's and g's. Here $\alpha_{n,F,G}^{1,2}$, $\beta_{n,F,G}^{1,2}$, $\gamma_{\mathrm{n,F,G}}^{1,2}$, $\lambda_{n,F,G}^{1,2}$, $\gamma_{n,C,D,F,G}^{2,1}$, and $\lambda_{\mathrm{n,C,\,D,\,F,\,G}}^{2,1}$ are zero within Eq. 47. Performing the matrix multiplication simplifies to:

$$\begin{pmatrix} C_n^1 \\ D_n^1 \end{pmatrix} = \begin{pmatrix} \tau_n & \varphi_n \\ \varsigma_n & \nu_n \end{pmatrix} \begin{pmatrix} C_n^1 \\ D_n^1 \end{pmatrix} \qquad 48)$$

$$0 = \begin{pmatrix} \tau_n - 1 & \varphi_n \\ \varsigma_n & \nu_n - 1 \end{pmatrix} \begin{pmatrix} C_n^1 \\ D_n^1 \end{pmatrix} \qquad 49)$$

The solution to Eq. 49 is either the trivial solution where the coefficients are zero or the determinant of the matrix containing the layer relation information being zero. The latter gives the dispersion relation for the entire system. Note, that the equation above contains all the information about each layer's dielectric properties, the thickness of each layer, the curvature for each layer, and the number of layers present.

IV. The Non-Radiative Regime

This chapter discusses results obtained in performing calculations for the non-radiative regime for the plasmon polariton dispersion (58). This is the regime to the right of the vacuum light line; alternatively, this is the area where $\chi_j^2 < 0$. In the definitions for the coefficients in Eqs. 31 - 46, both k and ω are real, and $\chi_j^2 = \frac{\varepsilon_j \mu_j}{c^2}\omega^2 - k^2$. In this case, $f=I(\chi_j\rho_j)$ and $g=K(\chi_j\rho_j)$ in Eqs. 31 – 46.

A number of parameters have been generalized for this system. For example, the system was imbedded in vacuum, thus $\varepsilon_0(\omega)=1$, the system is non-magnetic so μ is taken to be unity and the layer thickness, δ, is uniform for all layers. Previous studies (59, 60) have achieved good results for dielectric response properties of silver nanostructures when the form of the silver dielectric function for the layer material was taken to be:

$$\varepsilon(\omega) = \varepsilon_\infty - \frac{\omega_p^2}{\omega(\omega + i\gamma)} - \frac{\Delta_\varepsilon \Omega_L^2}{\omega^2 - \Omega_L^2 + i\Gamma\omega} \qquad 50)$$

Here, ε_∞ is dielectric constant of the material, ω_p the plasmon frequency, and γ is the electronic lifetime. The last term in Eq. 50 takes into account interband transitions and is fitted in order to obtain agreement with experimental data: the frequency, Ω_L, the strength, Δ_ε, and the spectral width of the Lorentz oscillator, Γ.

ε_∞	ω_p (THz)	Ω_L (THz)	Γ (THz)	Δ_ε	γ_{bulk} (THz)	v_F (m/s)	A
3.91	13420	6870	12340	.76	33.3	1.4E6	3

Table 2. Values of the optimized parameters used in the dielectric function to fit experimental data for silver (59, 60).

There are a couple of limiting cases for the dielectric function as described in Eq. 50. When all the damping parameters are taken to be zero, i.e. $\gamma = 0$ and $\Omega_L = 0$, the dielectric function models a perfect conductor. When $\Omega_L = 0$ but $\gamma \neq 0$, interband transitions are not taken into account and the material.

$$\gamma = \gamma_{bulk} + \frac{Av_F}{\delta} \qquad 51)$$

Eq. 51 shows the damping parameter used; δ is the layer thickness, v_f is the Fermi velocity, A is a constant taken to fit experimental data (61, 62). The additional damping term, γ_{bulk}, accounts for bulk damping; it accounts damping from interactions of electron-electron and electron-phonon. These additional scattering terms result from adjusting our system to fall within the nanoscale range where the size of our system is smaller then the electronic mean free path. Table 2 gives all the numerical values entered in $\varepsilon(\omega)$ for silver (59, 61).

The damping parameters γ and Γ make the dielectric function complex, thus the SPP frequency also becomes complex resulting in a time decay of the electric and magnetic fields. The real part of ω represents the energy of the SPP modes and the imaginary part of ω, which has a negative sign, represents the damping of the electromagnetic fields. Figure 3 shows the energy of the SPP excitations supported by the concentric cylindrical layers. The damping of the SPP modes is found to be at least three orders of magnitude smaller than the actual energy and its absolute value increasing with the increase of k. Here we only focus on the real part of $\omega(k)$.

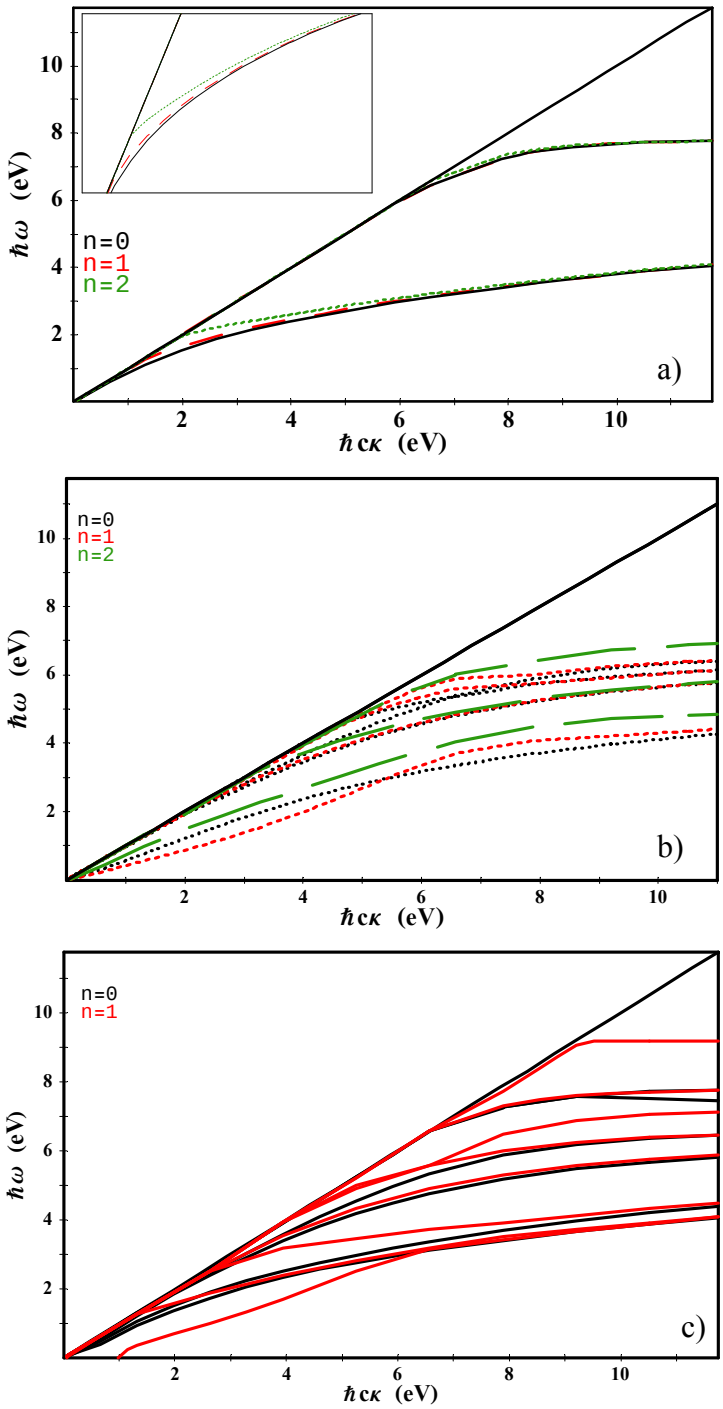

Figure 3. Energy dispersion of SPP modes as a function of wave vector *k*: a) one cylindrical layer (*N = 1) – R = 50 nm;* b) two cylindrical layers (*N=2) - R_1= 10 nm, R_2= 50 nm;* and c) three cylindrical layers (*N = 3) - R_1 = 10 nm, R_2 = 50 nm, R_3 = 90 nm*. The layer thickness is the same in each case - δ= 3 nm*. The plasmon energy is taken to be the same in each case - $\hbar\omega_p$ = 14 eV*. The straight line represents the light line $\omega = ck$.

The relation between number of layers and its dispersion curves is illustrated in Figure 3. The thickness was chosen to be the same for each layer and for each graph. In the $N = 1$ case, Figure 3a), each order of Bessel function is shown to have two modes. As the number of layers increases ($N = 2$ for Figure 3b) and $N = 3$ for Figure 3c)) the number of dispersion curves is shown to increase as well. This is attributed to the increase in the number of surfaces present, which in turn are able to support a larger number of modes. Similar results were obtained in previous studies conducted for thin slabs (63), cylinders with a dielectric core (37), and coated spherical shells (64).

Two sets of modes are clearly shown in Figure 3 for the one layered case. All the dispersions go to zero as the wave vector goes to zero as well. For one layer, each line is well defined; however, as the number of layers increase, the dispersions start to overlap, cross, or split suggesting strong interactions with the interfaces. A strong nonlinear behavior is seen at small wave vector values; nevertheless, this behavior is not seen at larger wave vector values as the behavior becomes dispersionless. As N increases, this nonlinear regime extends over a larger k region.

Different kinds of materials may influence the dispersion modes for a concentric cylindrical structure. To investigate this, a simple Drude formula for the dielectric function without damping and interband transitions was taken. By varying the characteristic plasmon frequency, ω_p, dependence on material can be investigated within the dispersion modes.

$$\varepsilon(\omega) = \varepsilon_\infty - \frac{\omega_p^2}{\omega^2} \qquad 52)$$

.

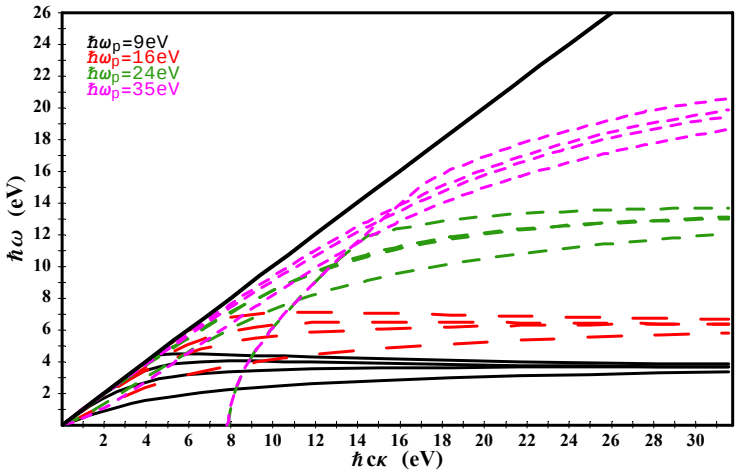

Figure 4. Energy dispersion for the lowest energy ($n = 0$) SPP eigenmodes of a system with $N = 2$ layers for different values of the plasma frequency. The radii are $R_1 = 10\ nm$ and $R_2 = 50\ nm$ and the thickness for each layer is $\delta = 3\ nm$. The light line $\omega = ck$ is also given.

Figure 4) shows the influence of varying the plasmon frequency for the dispersion modes. Each layer was to taken to be the same material, same thickness, same curvature, and surrounded by free space. As ω_p increases, it takes longer for the dispersion to plateau. This is attributed to the material acting more like a perfect conductor since the increase in ω_p increases the density of electrons. Also, for larger values of ω_p, the dispersion tends to stay somewhat parallel to the light line for longer periods in the wave vector. Ergo, for materials with larger plasmon frequency values, the excitations will experience retardation later when compared to materials with a smaller plasmon frequency.

Previous studies have shown curvature to be an important influence on the dispersion modes in a given system (37, 65 - 67). For example, the dispersion energetics for PPs change when one varies the size of a cylinder with a dielectric core (37) and the size for spherical systems (67). Decreasing the radius for each ring in a cylindrical array

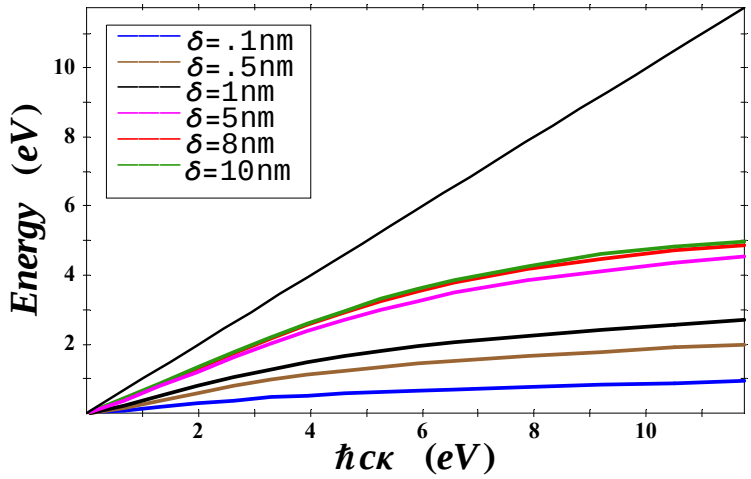

Figure 5. Energy dispersion for the lowest $n = 0$ eigenmode for different thicknesses. The system consists of two concentric layers with radii $R_1 = 10\ nm$ and $R_2 = 50\ nm$. The plasmon energy is $\hbar\omega_p = 14\ eV$. The light line is $\omega = ck$

imbedded in a metallic film has been shown to enhance optical transmission. Figures 5) and 6) will show that dispersion in the PP modes occurs for the system of concentric cylindrical layers. This is ascribed to curvature being a prominent feature when varying thickness and radii for a layered system.

Keeping the radii the same in a two layered system, Figure 5) shows the result of changing the thickness of each layer by the same amount. Only the lowest order, $n = 0$, is shown but similar results are obtained for higher order branches ($n = 1, 2, \ldots$). When the thickness is of magnitude smaller, the plateau in the dispersion occurs at a lower value for the wave vector. For thicknesses above half that of the smaller radii, the plateau takes longer to get to and the nonlinearity occurs until a lager wave vector value. Generally, as the thickness increases the modes for the PP excitations are pushed up into higher energetic values. Similar dependence on thickness have been shown for cylinders with a dielectric core (37). Unlike in that study, here we have examined a broader range and show greater variations in the dispersion as the variation takes place over a larger thickness range.

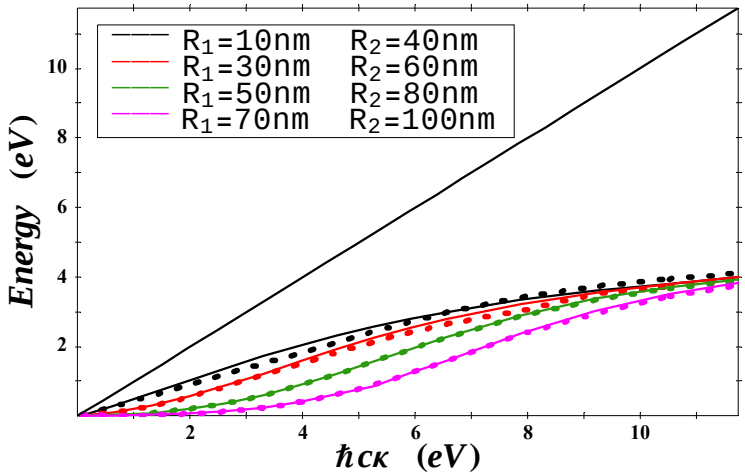

Figure 6. Energy dispersion for the lowest SPP eigenmodes for the $n = 0$ (solid line) and $n = 1$ (dashed line) branches. The thickness of each layer is δ= 3 nm and the plasmon energy is $\hbar\omega_p = 14\ eV$. The light line is $\omega = ck$

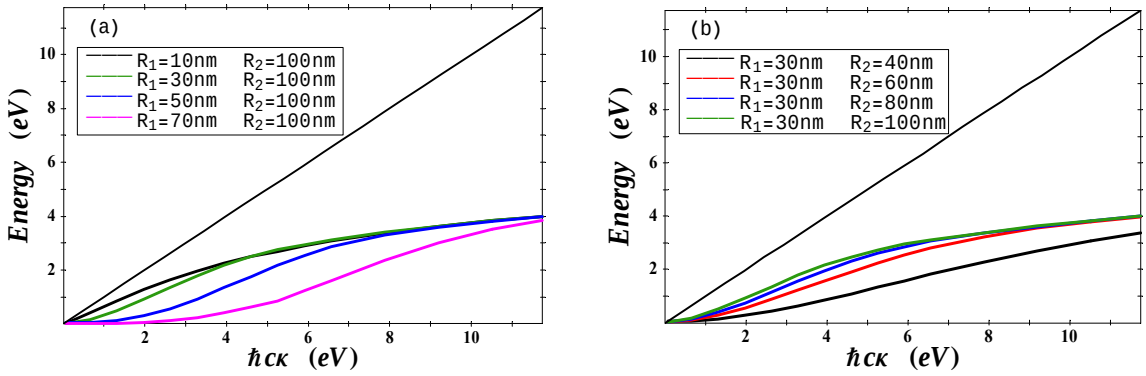

Figure 7. Energy dispersion for the lowest $n = 0$ SPP eigenmodes: a) the inner radius is varied; b) the outer radius is varied. The thickness of each layer is $\delta = 3\ nm$ and the plasmon energy is $\hbar\omega_p = 14$ eV. The light line is $\omega = ck$

Another way to influence the curvature of our system is to change the inner radii for the layers. This was investigated for a two layered system and the thickness of each layer was kept constant. Figure 6) demonstrates the effect of changing the inner radii of each layer for order $n = 0$ and $n = 1$. Both inner radii are taken to increase simultaneously. As the radii increases in the system, a la the curvature of the system decreases, the dispersion modes of the system have less energy then before. This occurs for both orders of the modes as they are seen to be very close in energy even overlapping

and crossing at certain points. Comparing this result with that from changing the thickness, one sees the opposite effect occurring. Therefore, two contending effects occur as one influences the curvature properties of a concentric multilayered cylindrical system.

As a final analysis, we investigated the effects of only changing one of the inner radii as the other was fixed. Thickness was also kept constant during the investigation for the lowest order of the two layered system. Figure 7a) shows the effects of changing the first inner radius, R_1, while varying the second inner radius, R_2. Figure 7b) displays shows the reverse, the first inner radius is fixed while the second inner radius is allowed to vary. By varying the radii this way, it provides a model of spacing two layers either closer or farther apart. When the two layers are closer to each other, the dispersion mode is decreased and a large area of nonlinearity appears. Nevertheless, at large wave vector values each dispersion approaches the same value. Figure 7) also shows different effects occur if the curvature of the system is change differently. In particular, when the first inner radius is decreased and the second kept fixed, $\omega(k)$ shifts up in energy. The reverse happens when R_1 is fixed and R_2 is allowed to decrease; $\omega(k)$ decreases in energy.

To sum up, several factors such as thickness of each layer, the radius of each layer, the overall radius of the system, and the proximity of the layers to each other influence the dispersion modes of a concentric cylindrical structure. As described earlier, varying these parameters leads to competing effects in the dispersion. Increasing the thickness of each layer (which brings the layers closer together) increases $\omega(k)$; however, if one varies the inner radii, R_1 and R_2, in such a way as to bring the layers closer, $\omega(k)$ decreases. If the difference between the inner radii is kept constant ($R_2 - R_1 = constant$),

but the overall curvature of the system decreases, $\omega(k)$ is suppressed. Similar results are obtained when one fixes R_2 but allows R_1 to increase; however, the opposite occurs to $\omega(k)$ when R_1 is kept constant but R_2 is allowed to increase.

Knowing that geometry greatly influences the dispersion modes for PPs in multilayered concentric cylinders and that by varying it's geometry one can take advantage of higher or lower PP modes should be a benefit to optical microscopic techniques. Scanning near-field optical microscopy uses tips which work for a specific mode (54, 68). To scan other modes, the size tip is varied or a coating applied. The results from this investigation show that one layered cylinders only have two modes available; however, if one would were to use a multilayered tip an increase in the range of modes would be accessible. Also, if the tip were needed to access a specific frequency, all that would be needed to be done is use different initial polarizations ($n = 0, 1, \ldots$) since the mode branches tend to be close or even overlap.

V. The Radiative Regime

The radiative regime deals with dissipative, radiating PP modes and a number of changes are needed within the model in order to accurately and aptly describe it. The radiative regime is the area to the left of the light line, $\omega = ck$, where $\chi_j^2 = k^2 - \frac{\varepsilon_j \mu_j}{c^2}\omega^2$. The wave vector, k, is still real; however, ω becomes complex, $\omega = \omega' + i\omega''$. In this regime, $f=J(\chi_j\rho_j)$ in Eqs. 31 - 46 and $g=H^1(\chi_j\rho_j)$; here H^1 is the first Hankel function $H^1=J(\chi_j\rho_j)+iN(\chi_j\rho_j)$.

The complex transcendental equation (Eq. 49) is solved again; therefore, no analytical solution is possible. Nevertheless, numerical evaluations are possible and this section discusses the results obtained (69) for carbon and silver nanocylinders. For silver, variations in layer thickness, number of layers, and change of the inner radii were considered when performing the calculations. For carbon nanotubes, number of layers and changing of the inner radii were considered.

First, we calculate the dispersion relations for a single silver layer. We examine the role of the size of the radial dimension of the layer in terms of its thickness and diameter. The dispersion relations for the real and imaginary parts are shown in Figure 8), where only the lowest level modes for the first three n are given. The light lines for this structure are determined by the vacuum: $\omega = kc$ (middle straight line), and by the silver material: $\omega\sqrt{\varepsilon_{Ag}(\omega)} = kc$ (6). The energy for each mode increases as the thickness δ (Figure 8a) or the radius R (Figure 8b) of the layer increases, showing that as

the curvature is decreased the modes approach the ones for a planar layer. Similar trend for ω_{Re} of the radiative modes was found for a full cylinder imbedded in vacuum (36). For larger *k*, the modes approach the silver light line indicating that they become more photon-like.

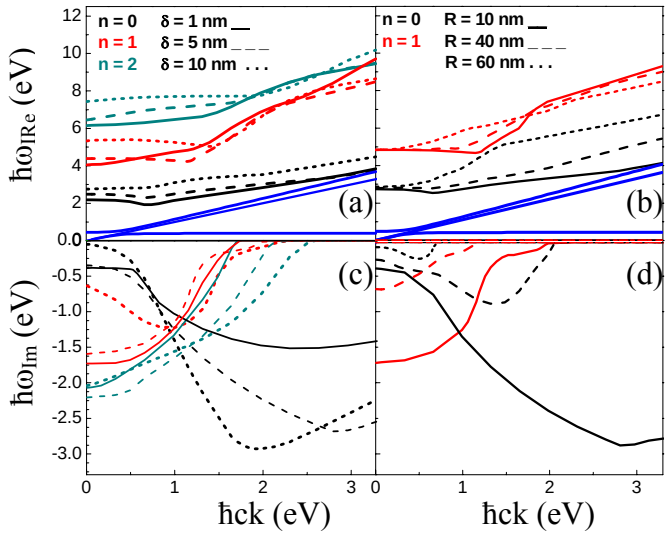

Figure 8. a) Real, and c) imaginary parts of the dispersion for *N=1* Ag layer for three values of the layer thickness and R = *10nm* b) real, and d) imaginary parts of the dispersion for *N = 1* Ag layer for several values of the radius and δ = 5 *nm*.

The imaginary part of the solutions for the modes are shown in Figures 8c) and 8d). Our results display a trend towards developing a deeper and relatively well pronounced minimum for $n = 0$ as the layer becomes thicker, thus showing the increase of damping for these modes. The imaginary part $|\omega_{Im}|$ for $n = 0$ mimics a similar behavior found for the lifetimes of these modes in a planar layer (6) when its thickness is increased. However, we find the opposite trend for $|\omega_{Im}|$ for $n = 0$ when the radius is increased, namely, $|\omega_{Im}|$ decreases as *R* increases showing a longer lived mode.

It is interesting to see that for $n = 1$ there is a minimum in ω_{Im} for a thicker layer while no such minimum is found for a thinner one – Figure 8c). Also, no such feature is obtained for the $n=2$ modes or for the $n=1$ for the specific δ in Figure 8d) when R is varied. In fact, for $R=60\ nm$, ω_{Im} is very small, thus the mode becomes well defined and long lived. In previous works (6, 36), the minimum in ω_{Im} has been associated in some cases with the existence of a Brewster angle for the particular modes. The Brewster angle is defined as the angle of incidence for which there is no reflected power of the electromagnetic waves in the structure (70). For cylindrical systems the angle is given as $\tan^2\varphi = \dfrac{k^2}{\omega^2/c^2 - k^2} = \varepsilon(\omega)$ (36). If the positions of maxima of ω_{Im} are in the close vicinity of the $\tan^2\varphi$ curve in the ω vs. k plane, then the mode is considered to be a Brewster mode. For $n=0$ ($\delta = 10\ nm$) and $n=1$ ($\delta = 10\ nm$) from Figure 8c), the modes minima are very close to the $\tan^2\varphi$ curve. The other minima for $n=0$ from Figure 8c) are found to be far away from $\tan^2\varphi$ curve. The $n=0$ (δ = 10 nm) mode in Figure 8d) is the only mode seen to have a minimum close to the $\tan^2\varphi$ line.

Our results show that both, the thickness and radius of the cylindrical layer, influence the radiative modes. A Brewster mode may or may not be found for a certain combination of R and δ. This is unlike the results for the radiative modes of a full cylinder, where Brewster modes exist for all n (36), and unlike the cases of planar layers for which the Brewster modes are determined by the initial polarization (6)

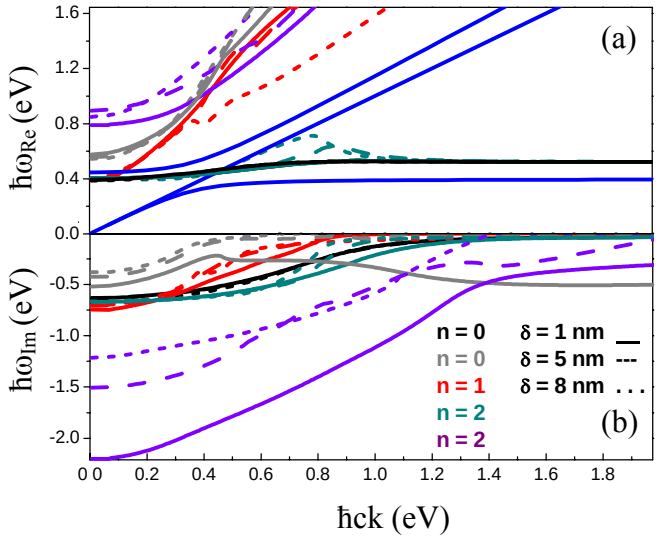

Figure 9. a) Real part and b) imaginary part of the dispersion for *N=2* Ag layers for three values of the thickness. The radii are $R_1 = 10nm$ and $R_2 = 20nm$.

In Figure 9 we show the results for the first and second lowest laying *n=0, 1, 2* modes of a system composed of two Ag layers for three values of the thickness. The energetics here appears more complicated as compared to the one layered system. This is attributed to the presence of more interfaces facilitating the scattering of the electromagnetic waves. An interesting behavior is found for the lowest *n=0, 2* modes for all δ . These start with relatively dispersionless $\hbar\omega_{Re}$ at ~ 0.4 eV just below the light line for Ag, then cross the vacuum light line, continuing into the regime of surface plasmon polaritons. The *n=0* modes are very close in energy for the different δ , while the ones for *n=2* show some differences in the $\hbar ck$ = 0.5-1.3 eV region. These particular modes have made the crossover from wave guided to non-radiative localized at the surfaces of the cylindrical structure. The crossover happens at a particular value of the wave vector where the argument of the Bessel and Hankel functions, χR, changes sign. Due to this argument sign change, a transformation to the modified Bessel functions I_n and

K_n occurs. Thus the dispersion relation equation now describes the non-radiative regime, however ω is still complex, therefore solutions for ω_{Im} are still possible. The lowest *n=1* excitations do not exhibit this behavior, they are entirely radiative. Such guided to surface electromagnetic excitations have also been found for planar multilayered materials (71), where their existence depends on the combination of the dielectric properties of the different materials involved. Our results show that the curvature and the number of layers in the system are also important.

Figure 9b) shows that $|\omega_{\mathrm{Im}}|$ for all *n* shows no minimum in its behavior, except the guided *n=0* exhibiting a shallow minimum at $\hbar ck \sim 1.7\ eV$. No Brewster mode is found here. Radiative modes with larger *n* are more heavily damped due to the larger values of $|\omega_{\mathrm{Im}}|$. The lifetime for the crossover modes for *n=0, 2* for the different δ does not show much deviation. $|\omega_{\mathrm{Im}}|$ decreases to very small values after $\hbar ck \sim 1.5\ eV$ indicating their non-radiative nature. The fact that $\omega_{\mathrm{Im}} \neq 0$ for these modes is explained by the existence of small losses in the Ag material due to γ_D and Ω_D.

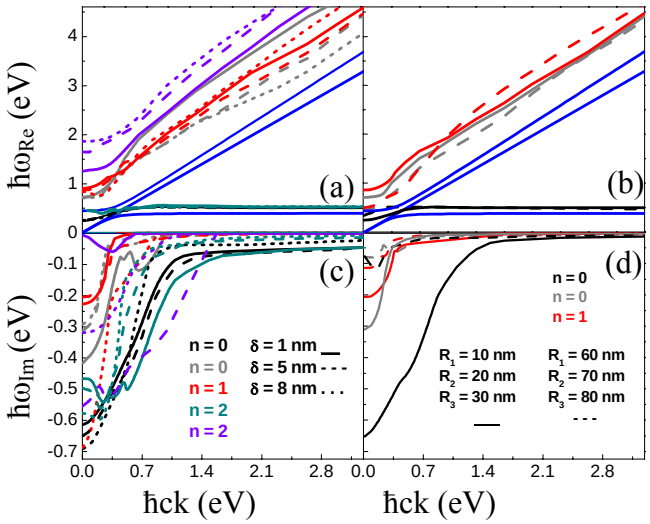

Figure 10. a) Real part, and c) imaginary parts for the dispersion of *N=3* Ag layers for several values of the layer thickness, $R_1 = 10$ *nm*, $R_2 = 20$ *nm*, $R_3 = 30$ *nm*; b) real, and d) imaginary parts of the dispersion for *N=3* Ag layers for several values of the radii and δ*=5 nm*.

Next, we consider a system composed of three Ag cylindrical layers. The role of thickness and overall radius size is investigated. In Figures 10a) and 10c), we show the dispersion relations of the two lowest laying *n=0, 1, 2* excitations for three values of the thickness. One sees again that the crossover wave guided to surface PP modes exist for *n=0, 2*, but not for *n=1* as in the case for *N=2* layers. For these, ω_{Re} does not show much difference for the different δ. Also, the thickness does not seem to influence significantly the low *k* regime for ω_{Re} for the radiative *n=0, 1* modes, where the energy is almost the same for all δ. The overall size of the system affects the low *k* regime, where for the larger radii (Fig. 10b) the modes are higher in energy as compared to the ones for the smaller radii. At larger *k* they all become almost parallel to the Ag light line with ω_{Re} being slightly higher.

The results from Figure 10c) show that for some *n* and δ, ω_{Im} can have local minima at a specific wave vector *k*. For example, for the radiative *n=0,* a local minimum

is found at $\hbar ck \sim 0.65$ eV, $\delta = 1$ nm and $\hbar ck \sim 0.3$ eV, $\delta = 8$ nm. On the other hand, for the radiative $n=2$ only a global minimum is found at $\hbar ck \sim 0.25$ eV. One also sees that as the overall size of the system is varied from having larger curvature to having smaller curvature, the dispersion for ω_{Re} does not change much. However, the modes are more heavily damped for the structure with larger curvature (smaller layer radii).

Further, we consider concentric cylindrical layers made out of carbon in an attempt to model the radiative PP excitation spectrum in carbon nanotubes. Several studies related to mechanical and optical properties have shown that in many instances carbon nanotubes behave similarly as continuous cylindrical structures (72 – 75). Thus it becomes eminent that such continuous models can be a relatively fast tool for useful analysis of their properties. Here we assume that the separation between the layers in the carbon concentric cylindrical structure is of the same order as the equilibrium distance in multiwalled carbon nanotubes ~ 3.5 Å (72). Calculations for the dispersion spectra for other thicknesses ranging from $\delta = 1$ *nm* to $\delta = 2$ *nm* were done and the results showed to be very similar, therefore we present only the radiative PP for $\delta = 1.5nm$.

For the dielectric function we also employ an effective dielectric function expression similar to the Eq. (50) with a combination of a Drude term and localized Lorentzian absorption peaks:

$$\varepsilon(\omega) = \varepsilon_{\infty} - \frac{\omega_D^2}{\omega(\omega + i\gamma_D)} - \sum_j \frac{\Omega_{pj}^2}{(\omega^2 - \omega_j^2) + i\Gamma_j \omega} \qquad 53)$$

ε_c	ω_p (eV)	Ω_{pj} (eV)	ω_j (eV)	Γ_j (eV)	γ (eV)
8.5	0.64	0.45	0.02	0.042	0.25

Table 3. Values of the parameters used in the dielectric function for carbon nanotubes (31).

The values for the frequency independent dielectric constant ε_∞, plasma frequency ω_D, carrier relaxation rate γ_D, Lorentzian central frequency ω_{pj}, strength of each Lorentzian oscillator Ω_{pj}, and spectral width of each Lorentzian oscillator Γ_j, are listed in Table 3, where the optical spectrum of a film of carbon nanotube was measured and modeled successfully using the effective expression from Eq. 53).

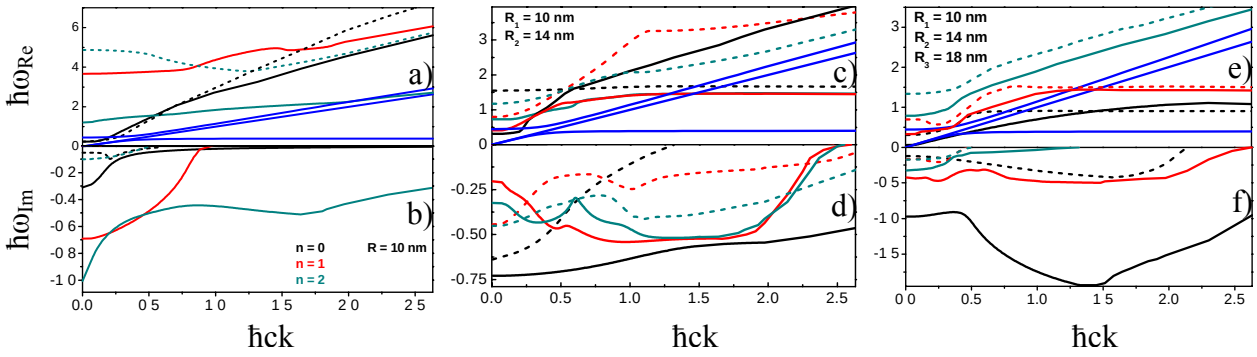

Figure 11. Real part of the dispersion for a) $N = 1$; c) $N = 2$; e) $N = 3$ layers. Imaginary part of the dispersion for b) $N = 1$; d) $N = 2$; f) $N = 3$ layers. The thickness in each case is $\delta = 1.5\ nm$.

Figure 11 displays the results for the lowest lying modes for a system with $N=1, 2, 3$ carbon layers. For one layer, crossover guided modes are found only for $n=0, 2$. However, for $N=2, 3$ such modes are found for all n. Some features such as local minima and maxima are found in ω_{Im} for $N=2$ and $N=3$ layers. These are attributed to the presence of more scattering interfaces and their closeness. Due to the smaller damping constant γ for the carbon system (58, 75), the modes tend to be less damped as compared to those for silver layers with comparable sizes. These results also show that materials characterized with different dielectric functions can have different effect on the dispersion of the electromagnetic modes of a system with compatible structure characteristics. For example, for Ag $N=1$ ω_{Im} exhibits minima for different n, but for C $N=1$, ω_{Im} does not with the exception of the second $n=0$ mode as seen in Figure 11b).

Also, for *N=3* all studied modes of the Ag system show significant damping over a shorter wave vector range as compared to the ones for a C system. The broad minima found in Figures 11d) and 11f) for some *n* aren't associated with the $\tan^2\varphi$ curve.

VI. Conclusions

In conclusion, I have presented a simple model to calculate the energy dispersion relation of the radiative and non-radiative plasmon polariton modes of a multilayered infinitely long cylindrical system. The final expression for the dispersion is obtained by solving the Maxwell's equations with appropriate boundary conditions and it is written in a matrix form. It takes into account the finite speed of light, the dielectric properties of the materials, the number of layers, and their curvature.

The general expressions presented here can be used for other studies as well. For example, all or some layers can be made to have different thickness and/or different dielectric properties (different ω_p). The system can also be submerged in to an environment with $\varepsilon_0(\omega) \neq 1$. Thus multilayered cylindrical structures provide many ways of tailoring the optical properties of nanostructures demonstrating their versatility in optical applications.

The results from the non-radiative regime show that the surface plasmon polariton spectrum becomes more complex as the number of layers increases. In the multilayered cylindrical system, the energy subbranches for each branch n are a result from strong interaction between electromagnetic oscillations from all interfaces. Many of the modes from different n can cross each other, split into subbranches at a particular wave vector or overlap. Such complexity, particularly the closeness of the branches, might make it difficult to distinguish them experimentally. On the other hand, if a specific mode range is needed, the excitation can be done with different initial polarizations. The numerical

evaluations for the $N = 2$ case indicate that varying the dielectric properties, the thickness, and/or the size of one or both layers can change the SPP modes energy significantly. We demonstrate that the SPP energy can be red-shifted or blue-shifted in different ways simply by modifying the size and curvature of the systems.

For the radiative regime, specific calculations were done for a system composed of silver or carbon layers. The dielectric function for each material is taken from available experimental measurements, and it includes a Drude-like contribution and interband optical transitions. We find that some modes are more heavily damped than other. Also, for some systems crossover modes from the radiative region to the guided region can be found. Our results show that the energy spectra are complex resulting from the interplay between the number of layers, their proximity and the dielectric function parameters, but due to the rather technically involved expression for the energy spectrum implicit conclusions are not possible. However, our method can be easily applied to any system consisting of cylindrical layers submerged into a medium with different structural and dielectric characteristics. Thus many ways of tailoring the plasmon polariton properties of such nanostructures can be achieved for appropriate experimental applications.

These kinds of cylindrical structures may find applications in scanning near-field optical microscopy where they would be used as the scanning tips. There are many advantages as indicated by our results for doing this: more modes are available for excitations, thus greater range of operation; a range of excitations can be excited by different initial polarizations; blue shifting and red shifting if the dispersion spectra can be achieved in many more ways as compared to using just coated cylindrical tips, thus

there are many more possibilities for engineering the system for the desired range of operation.

References

(1) U. Fano, J. Opt. Soc. Am. **31**, 213 (1941).

(2) K. L. Ngai, E. N. Economou, and M. H. Cohen, Phys. Rev. Lett. **24**, 61 (1970).

(3) J. G. Endriz and W. E. Spicer, Phys. Rev. Lett. **24**, 64 (1970).

(4) J. J. Lander and J, Morrison, Surf. Sci. **14**, 465 (1969).

(5) R. Fuchs and K. L. Kliewer, Phys. Rev. **140**, A2076 (1965).

(6) K. L. Kliewer and R. Fuchs, Phys. Rev. **150**, 573 (1966).

(7) D. E. Beck and V. Celli, Phys. Rev. Lett. **28**, 1124 (1972).

(8) P. Gadenne, M. Gadenne, J. Lafait, P. Sheng, M. Zhou, and A. F. Ruppert, Europhys. Lett. **27**, 623 (1994).

(9) J. K. Jain and P. B. Allen, Phys. Rev. Lett. **54**, 2437 (1985).

(10) H. Welsch and J. Lafait, Opt. Comm. **116**, 369 (1995).

(11) E. Prodan and N. Nordlander, J. of Chem. Phys. **120**, 5444 (2004).

(12) J. A. Sánchez-Gil and A. A. Maradudin, Phys. Rev. B. **60**, 8359 (1999).

(13) C. J. Powell and J. B. Swan, Phys. Rev. **120**, (1960).

(14) G. Flätgen, K. Krischer, B. Pettinger, K. Doblhofer, H. Junkes, and G. Ertl, Science **269**, 668 (1995).

(15) M. Malmqvist, Nature **261**, 186 (1993).

(16) W. Knoll, Ann. Rev. Phys. Chem. **49**, 3755 (1998).

(17) A. Otto, Z. Phys. **216**, 398 (1968).

(18) E. Kretschmann and H. Raether, Z. Naturforsch. AZ. Naturforsch. **23**, 2135 (1968).

(19) R. A. Innes and J. R. Sambles, J. Phys. F: Met. Phys. **17**, 277 (1987).

(20) J. Liang, H. Chik, A. Yin, and J. Xu, J. of App. Phys. Comm. **91**, 2544 (2002).

(21) Y. J. Park, J. G. Kim, M. K. Kim, H. T. Chung, W. S. Um, M. H. Kim, and H. G. Kim, J. of Power Sources, **76**, 41 (1998)**.**

(22) J. Kim, Y. Kim, Y. S. Kim, J. Lee, L. Kim, and D. Jung, App. Phys. Lett. **80**, 3581 (2002).

(23) M. Yu, O. Lourie, M. J. Dyer, K. Moloni, T. F. Kelly, and R. S. Ruoff, Science **287**, 637 (2000).

(24) A. M. Morales and C. M. Lieber, Science **279**, 208 (1998).

(25) S. Iijima, Lett. to Nature **354**, 7 (1991).

(26) Y. Xia, P. Yang, Y. Sun, Y. Wu, B. Mayers, B. Gates, Y. Yin, F. Kim, and H. Yan, Adv. Mat. **15**, 353 (2003).

(27) L. Shao, D. Caruntu, J. F. Chen, C. J. O'Connor, and W. L. Zhou, J. of App. Phys. **97**, 10Q908 (2005).

(28) K. Liu, J. Nogués, C. Leighton, H. Masuda, K. Nishio, I. V. Roshchin, and I. K. Schuller, App. Phys. Lett. **81**, 4434 (2002).

(29) D. R. Larson, W. R. Zipfel, R. M. Williams, S. W. Clark, M. P. Bruchez, F. W. Wise, and W. W. Webb, Science **300**, 1434 (2003).

(30) K. Aslan, M. Wu, J. R. Lakowicz, and C. D. Geddes, J. of Fluor. **17**, 127 (2007).

(31) A. Ugawa, A. G. Rinzler, and D. B. Tanner, Phys. Rev. B **60**, R11 305 (1999).

(32) M. Laroche, S. Albaladejo, R. Gómez-Medina, and J. J. Sáenz, Phys. Rev. B. **74**, 245422 (2006).

(33) C. A. Pfeiffer, E. N. Economou, and K. L. Ngai, Phys. Rev. B **10**, 3038 (1974).

(34) M. Krčmar, W. M. Saslow, and A. Zangwill, J. App. Phys. **93**, 3495 (2003).

(35) D. L. Bullock and G. Oltman, Phys. of Fluids **9**, 2026 (1966).

(36) S. S. Martinos and E. N. Economou, Phys. Rev. B **28**, 3173 (1983).

(37) U. Schröter and A. Dereux, Phys. Rev. B **64**, 125420 (2001).

(38) V. A. Parsegian and G. H. Weiss, J. of Chem. Phys. **60**, 5080 (1974).

(39) H. Khosravi, D. R. Tilley, and R. Loudon, J. Opt. Soc. Am. A **8**, 112 (1991).

(40) T. Guo, P. Nikolaev, A. Thess, D. T. Colbert, and R. E. Smalley, Chem. Phys. Lett. **243**, 49 (1995).

(41) A. A. Setlur, S. P. Doherty, J. Y. Dai, and R. P. H. Chang, App. Phys. Lett. **76**, 3008 (2000).

(42) S. J. Oldenburg, R. D. Averitt, S. L. Westcott, and N. J. Halas, Chem. Phys. Lett. **288**, 243 (1998).

(43) C. F. Herrmann, F. H. Fabreguette, D. S. Finch, R. Geiss, and S. M. George, App. Phys. Lett. **87**, 123110 (2005).

(44) J. T. Boyd, *Progress in Lasers and Electro-Optics*. (The Institute of Electrical and Electronics Engineering, New York, 1991).

(45) T. Katsuyama and K. Ogawa, J. of Appl. Phys. **75**, 7607 (1994).

(46) L. Salomon, F. Grillot, A. V. Zayats, and F. de Fornel, Phys. Rev. Lett. **86**, (2001).

(47) E. Ozbay, Science **311**, 189 (2006).

(48) B. E. Sernelius, *Surface Modes in Physics*. (Wiley-VCH, Germany, 2001).

(49) H. B. G. Casimir, Proc. K. Ned. Akad. Wet. **51**, 793 (1948).

(50) N. W. Ashcroft and N. D. Mermin, *Solid State Physics*. (Thomson Learning Inc., 1976).

(51) M. Schubert, T. Hofmann, J. Šik, Phys. Rev. B. **71**, 035324 (2005).

(52) G. F. Craven and C. K. Mok, Trans. on Micro. Th. and Tech. **19**, 295 (1971).

(53) M. Sarrazin and J. P. Vigneron, Phys. Rev. B **71**, 075404 (2005).

(54) L. Novotny, D. W. Pohl, B. Hecht, Ultramicroscopy **61**, 1 (1995).

(55) M. Specht, J. D. Pedaring, W. M. Heckl, and T. W. Hänsch, Phys. Rev. Lett. **68**, 476 (1992).

(56) K. Tatur, L. M. Woods, and I. V. Bondarev, Phys. Rev. A **18**, 012110 (2008).

(57) E. T. Arakawa, M. W. Williams, R. N. Hamm, and R. H. Ritchie, Phys. Rev. Lett. **31**, 1127 (1973).

(58) J. Pritz and L. M. Woods, S. St. Comm. **146**, 345 (2008).

(59) T. Laroche, and C. Girard, Appl. Phys. Lett. **89**, 233119 (2006).

(60) A. Vial, A. Grimault, D. Macías, D. Barchiesi, and M. L. de la Chapelle, Phys. Rev. B **71**, 085416 (2005).

(61) S. L. Westcott, J. B. Jackson, C. Radloff, and N. J. Halas, Phys. Rev. B **66**, 155431 (2002).

(62) U. Kreibig and M. Vollmer, *Optical Properties of Metal Clusters*. (Springer, Germany, 1995).

(63) R. H. Ritchie, Phys. Rev. **106**, 874 (1957).

(64) D. Ugarte, C. Colliex, and P. Trebbia, Phys. Rev. B **45**, 4332 (1992).

(65) M. I. Haftel, C. Schlockermann, and G. Blumberg, Phys. Rev. B **74**, 235405 (2006).

(66) M. I. Haftel, C. Schlockermann, and G. Blumberg, Appl. Phys. Lett. **88**, 193104 (2006).

(67) A. Passian, R. H. Ritchie, A. L. Lereu, T. Thundat, and T. L. Ferrell, Phys. Rev. B **71**, 115425 (2005).

(68) J. Koglin, U. C. Fischer, and H. Fuchs, Phys. Rev. B **55**, 7977 (1997).

(69) J. Pritz and L. M. Woods, under review at Physica B

(70) J. D. Jackson, *Classical Electrodynamics*. (John Wiley & Sons, USA, 1999).

(71) M. A. Gilmore and B. L. Johnson, J. Appl. Phys. **93**, 4497 (2003).

(72) T. Vodenitcharova and L. C. Zhang, Phys. Rev. B **68**, 165401 (2003)

(73) G. Gumbs and G. R. Aĭzin, Phys. Rev. B **65**, 195407 (2002).

(74) F. J. García-Vidal, J. M. Pitarke, and J. B. Pendry, Phys. Rev. B **58**, 6783 (1998).

(75) J. P. Salvetat, J. M. Bonard, N. H. Thomson, A. J. Kulik, L. Forró, W. Benoit, and L. Zuppiroli, Appl. Phys. A **69**, 255 (1999).

Bibliography

I. Breukelaar and P. Berini, J. Opt. Soc. Am. A **23** 081971 (2006)

J. M. Pitarke, V. M. Silkin, E. V. Chulkov, and P. M. Echenique, Rep. Prog. Phys. **70** 1 (2007)